
RAM-W600: A Multi-Task Wrist Dataset and Benchmark for Rheumatoid Arthritis

Songxiao Yang^{1*} Haolin Wang^{2*} Yao Fu² Ye Tian³ Tamotsu Kamishima²
Masayuki Ikebe² Yafei Ou^{1†} Masatoshi Okutomi¹

¹ Institute of Science Tokyo, Tokyo, Japan

² Hokkaido University, Sapporo, Japan

³ The University of Tokyo, Tokyo, Japan

Abstract

Rheumatoid arthritis (RA) is a common autoimmune disease that has been the focus of research in computer-aided diagnosis (CAD) and disease monitoring. In clinical settings, conventional radiography (CR) is widely used for the screening and evaluation of RA due to its low cost and accessibility. The wrist is a critical region for the diagnosis of RA. However, CAD research in this area remains limited, primarily due to the challenges in acquiring high-quality instance-level annotations. (i) The wrist comprises numerous small bones with narrow joint spaces, complex structures, and frequent overlaps, requiring detailed anatomical knowledge for accurate annotation. (ii) Disease progression in RA often leads to osteophyte, bone erosion (BE), and even bony ankylosis, which alter bone morphology and increase annotation difficulty, necessitating expertise in rheumatology. This work presents a multi-task dataset for wrist bone in CR, including two tasks: (i) wrist bone instance segmentation and (ii) Sharp/van der Heijde (SvdH) BE scoring, which is the first public resource for wrist bone instance segmentation. This dataset comprises 621 wrist conventional radiographs of 227 patients from four medical centers, with pixel-level instance segmentation annotations for 443 images and SvdH BE scores for 548 images. This dataset can potentially support a wide range of research tasks related to RA, including joint space narrowing (JSN) progression quantification, BE detection, bone deformity evaluation, and osteophyte detection. It may also be applied to other wrist-related tasks, such as carpal bone fracture localization. We hope this dataset will significantly lower the barrier to research on wrist RA and accelerate progress in CAD research within the RA-related domain.

🔗 **Benchmark & Code:** github.com/YSongxiao/RAM-W600

📄 **Data & Dataset Card:** huggingface.co/datasets/TokyoTechMagicYang/RAM-W600

1 Introduction

The wrist is a highly complex joint that facilitates a wide range of motion and bears substantial mechanical loads during daily activities. Due to its anatomical complexity and functional demands, the wrist is particularly susceptible to various pathological conditions [15]. Among these, rheumatoid arthritis (RA) is a common and debilitating autoimmune disease that frequently affects the wrist joint early in its progression [56]. It is marked by joint swelling and tenderness, which progressively leads to joint destruction and significant disability. Radiographic analysis plays a pivotal role in the diagnosis and management of RA, with joint space narrowing (JSN) progression and bone erosion (BE) serving as key markers for evaluating and tracking disease progression [1, 49]. However, traditional radiographic assessment heavily relies on the radiologist’s expertise and subjective interpretation

*Equal Contribution.

†Corresponding Author (ou.y.ac@m.titech.ac.jp)

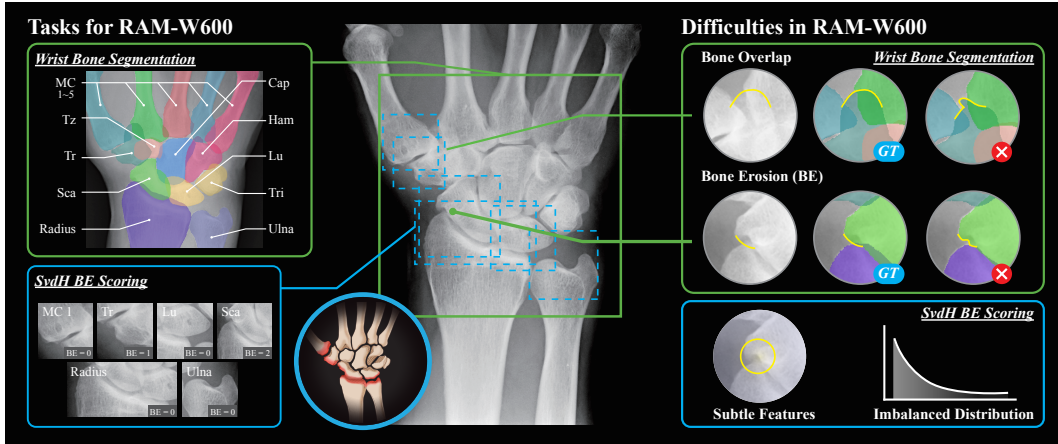


Figure 1: Overview of the RAM-W600 dataset, designed for wrist bone segmentation and SvdH BE scoring tasks. (MC 1 to 5: Metacarpal 1 to 5; Tz: Trapezoid; Tr: Trapezium; Sca: Scaphoid; Radius: DistalRadius; Cap: Capitate; Ham: Hamate; Lu: Lunate; Tri: Pisiform & Triquetrum; Ulna: DistalUlna)

to detect subtle pathological features, which is time-consuming and often associated with limited accuracy and sensitivity. As a result, the development of computer-aided diagnostic (CAD) systems has attracted growing interest from both academic and industrial communities [58, 32, 67, 68].

Accurate segmentation of wrist bones is critically important in medical image analysis, as it serves as a foundational step for numerous downstream tasks essential to the diagnosis and management of RA. These tasks include, but are not limited to, the evaluation of bone deformities, detection of osteophytes, and assessment of JSN. For example, in bone deformity analysis, precise segmentation is required to extract geometric features such as bone angles, alignment, and morphological irregularities across longitudinal scans [27]. In osteophyte detection, segmented bone contours help identify abnormal bony outgrowths that are often hard to distinguish in raw radiographs due to anatomical overlap [48]. Similarly, accurate quantification of JSN depends on the precise boundaries between adjacent bones [30, 47, 69]. Segmentation errors can lead to incorrect inter-bone distance measurements, which are essential for monitoring disease progression.

However, the annotation process of a large-scale dataset is highly challenging and labor-intensive due to the anatomical complexity of the wrist and different pathological changes in the wrist bones. As shown in Fig. 1, (i) Obscured edges due to overlapping structures. The wrist, a structurally complex joint system, features tightly interlocked carpal bones [4]. This configuration frequently leads to overlapping phenomena in conventional radiography (CR), which significantly complicates the identification of each bone's outer edges. (ii) Morphological alterations resulting from pathological conditions. Due to the progression of RA and other pathological changes, BE, JSN, and osteophyte formation can affect certain bones or joints to varying degrees, often leading to substantial alterations in bone morphology [61, 16, 28]. Moreover, these factors may interact in diverse and combinatorial ways, further complicating the consistency and accuracy of annotations.

Sharp/van der Heijde (SvdH) BE scoring [64] is a widely recognized task in the automated diagnosis of RA. Nevertheless, it remains highly challenging due to difficulties in both annotation and model training. On the annotation side [52, 65], (i) accurate annotation demands specialized rheumatological expertise, as assessing the severity of BE is inherently complex. (ii) The process is subjective and prone to substantial inter-observer variability, resulting in inconsistent and uncertain ground truth labels. This subjectivity and ambiguity undermine the quality of supervision available for model training. From a training perspective, (i) the task is further complicated by a severe class imbalance, as cases of high-grade erosion are underrepresented in most clinical datasets. (ii) The pathological features of BE are often subtle, highly localized, small in scale, and demonstrating minimal variation across severity levels, thereby posing substantial challenges for automated detection and classification. Collectively, these factors render SvdH BE scoring a challenging task in developing robust and generalizable deep learning models for RA assessment.

Table 1: Comparison between RAM-W600 and the publicly available annotated datasets. Ann/Img: Annotations per image.

Modality	Dataset	Year	Images (Ann/Img)	Resolution (mm/pixel)	Age (Mean±SD)	Tasks		Purpose
						Mask	Score	
CR	Halabi et al. [22]	2019	14236 (15)	-	0.35	✓		BAA
	Sun et al. [59]	2022	674 (31)	-	-		✓	RA
	Ours (RAM-W600)	2025	443 (15) + 548 (6)	0.15	44.99±20.94	✓	✓	RA
CT	Moore et al. [43]	2007	30 (15)	-	26.25±3.33	✓		-

BAA: Bone Age Assessment.

In this paper, we introduce **Rheumatoid Arthritis Modeling-Wrist 600 (RAM-W600)**, a multi-task dataset for wrist bone in conventional radiography. It comprises 621 wrist conventional radiographs of 227 patients from four medical centers. Among them, 443 high-resolution wrist radiographs are provided with expert-verified instance-level annotations for wrist bone segmentation, along with 3288 SvdH BE scores. This dataset is expected to support a wide range of downstream tasks, such as anatomical structure localization, erosion progression analysis, and automated disease staging, thereby contributing to the broader advancement of computer-aided diagnosis in RA. Our primary contributions are threefold:

- **First Multi-Task dataset for RA:** RAM-W600 is the first public large-scale dataset dedicated to both segmentation and SvdH BE scoring tasks, providing a valuable benchmark for developing and validating deep learning algorithms in conventional radiographs. Its multi-institutional composition ensures diversity in acquisition conditions, enhancing the generalizability of trained models.
- **High-quality annotations:** We provide high-quality pixel-level annotations of the wrist bones, including careful handling of overlapping region boundaries, and SvdH BE score in the region of interest (ROI).
- **Comprehensive benchmarks:** We present a benchmark for wrist bone instance segmentation and SvdH BE scoring, enabling standardized evaluation and comparison of algorithms for automated RA assessment.

2 Related Works

2.1 Hand Radiographic Datasets

Although hand radiographic data are relatively easy to acquire, the complex anatomical structure of the hand and the inherent limitations of current imaging techniques present significant challenges for accurate annotation. As shown in Table 1, these challenges are further intensified in disease-specific applications, such as the diagnosis and monitoring of RA, where high-quality, expert-annotated datasets remain scarce. Earlier efforts produced computed tomography (CT) datasets with segmentation masks [43], but these were limited by small sample sizes. More recently, Halabi et al. [22] released a large-scale CR dataset annotated with segmentation masks; however, its utility is confined to pediatric bone age assessment and limited to selected phalangeal regions. In contrast, RA-specific datasets such as that of Sun et al. [59] provide severity scores but lack pixel-wise annotations, thereby constraining their applicability to tasks requiring precise image segmentation.

2.2 Wrist Bone Segmentation

Radiological analysis of the wrist bones is central to the study of hand-related disorders. In particular, image segmentation plays an important role and holds significant value for both clinical practice and research, as summarized in Table 2. Notable progress has been made in wrist bone segmentation using various imaging modalities, including CT and magnetic resonance imaging (MRI). Early studies employed mathematical modeling techniques to achieve relatively mature segmentation outcomes on CT and MRI scans [3, 18]. With recent advances in deep learning, both 2D and 3D segmentation of wrist bones in CT and MRI has further matured [72, 62, 50, 55, 51], enabling more specialized investigations into disease-induced bone pathologies. In contrast, research on wrist bone segmentation

Table 2: Summary of recent works on wrist segmentation. Ann/Img: Annotations per image.

Modality	Works	Year	Backbone	Dataset	Images (Ann/Img)	Age (Mean±SD)	Objects			Purpose
							F	C	UR	
CR	Yang et al. [71]	2021	ResNet	Private	720 (2)	36±13		✓		BMD
	Kang et al. [31]	2022	Mask R-CNN	Private	702 (10)	-	✓	✓		-
	Lee et al. [33]	2023	SAM	Private	192 (7)	-	✓		✓	BMD
	Du et al. [14]	2024	GRU-UNet	[22] & Private	2000 (13)	-	✓	✓	✓	BAA
CT	Anas et al. [3]	2016	-	[43] & Private	60 (15)	-	✓	✓	✓	-
	Sebro et al. [55]	2022	-	Private	196 (17)	64.9±8.7	✓	✓	✓	BMD
4DCT	Teule et al. [62]	2024	nnU-Net	Private	19 (9)	-		✓	✓	-
MRI	Foster et al. [18]	2018	-	Private	160 (8)	47.1±9.25		✓		OA
	Radke et al. [50]	2021	CNN	Private	56 (8)	30.7±13.6		✓	✓	LWI
	Yiu et al. [72]	2024	nnU-Net	Private	80 (15)	54±12	✓	✓	✓	RA(BME)
	Raith et al. [51]	2025	3D U-Net	Private	15 (8)	27.8±3.11		✓		-

F: Finger Bones; **C**: Carpal Bones; **UR**: Radius and Ulna Bones;
BMD: Bone Mineral Density; **BAA**: Bone Age Assessment;
RA(BME): Rheumatoid Arthritis with Bone Marrow Edema; **LWI**: Ligamentous Wrist Injuries.

Table 3: Summary of recent works on RA-related scoring. Ann/Img: Annotations per image.

Modality	Works	Year	Backbone	Dataset	Images (Ann/Img)	Patients	Age (Mean±SD)	Tasks	
								SvdH BE	Others
CR	Hirano et al. [25]	2019	CNN	Private	216 (15)	108	64.9±4.87	✓	SvdH JSN
	Ureten et al. [63]	2020	CNN	Private	180 (2)	180	-		RA & HC
	Maziarz et al. [40]	2021	Unet	[59]	674 (31)	562	-		Damage
	Hioki et al. [24]	2021	Yolo V3	Private	50 (4)	-	-		Destruction
	Miyama et al. [42]	2022	DNN	Private	226 (31)	40	61.5±11.6	✓	SvdH JSN
	Wang et al. [66]	2022	Yolo	Private	915 (30)	400	>20		mTSS
	Sun et al. [59]	2022	DNN	[59]	674 (31)	562	-	✓	SvdH JSN
	Bo et al. [5]	2024	ResNet	Private	3818 (10)	-	-	✓	SvdH JSN
Lien et al. [36]	2025	Yolo V7	Private	823 (30)	-	>20		mTSS	
HR-pQCT	Folle et al. [17]	2022	GradCAM	Private	932 (3)	617	45±15		HC & RA & PsA
MRI	Schlereth et al. [54]	2024	CNN	Private	211 (66)	112	54.1±12.4	✓	osteitis & synovitis

mTSS: modified total Sharp Score; **PsA**: psoriatic arthritis; **HC**: healthy controls.

from radiographs is still limited. Although several deep learning-based methods have been proposed [71, 31, 14, 33], few studies focus on complex pathological conditions such as RA. This may be due to the limitations of CR. Its two-dimensional nature causes anatomical overlap, tissue superposition, and low contrast, which make it difficult to identify bone boundaries and anatomical structures. In addition, although CR is more accessible and cost-effective than CT or MRI, accurate annotation is still difficult, especially in cases with active osteoarticular lesions. As a result, there are few high-quality, publicly available annotated datasets. This lack of data makes it hard to train and evaluate reliable segmentation models.

Consequently, achieving high-precision wrist bone segmentation in radiographs of patients with complex pathological conditions remains a critical challenge. Addressing this issue holds substantial potential for advancing efficient and user-friendly clinical decision support systems.

2.3 Detection and Assessment of BE

The SvdH scoring system has been widely used to evaluate various joint abnormalities in RA. As summarized in Table 3, an increasing number of automated methods have been developed in recent years to facilitate RA radiograph scoring. These approaches are typically based on the SvdH system and aim to assess key indicators such as JSN, BE, and the modified total Sharp score (mTSS). Most models are trained and validated on private datasets. Earlier studies primarily employed convolutional neural networks (CNNs) for feature extraction and classification [26, 42, 59, 5]. Recently, object detection-based models have been introduced [24, 36], enabling the integration of lesion localization and scoring within end-to-end pipelines and enhancing both automation and usability. Some studies have explored RA classification and severity assessment using scoring systems other than SvdH [63, 40, 24]. Furthermore, research on automated RA assessment has expanded to encompass various imaging modalities, including MRI [54] and high-resolution peripheral quantitative computed tomography (HR-pQCT) [17], along with the investigation of alternative scoring methods and evaluation standards, thereby further advancing the field of RA imaging analysis.

In summary, the wrist joint is one of the most anatomically complex and diagnostically significant regions in RA radiograph, offering substantial clinical and research value. Notably, the integration of precise wrist bone segmentation and lesion scoring within a multi-task learning framework has emerged as a key direction in advancing automated RA analysis. However, publicly available hand CR datasets remain significantly limited, particularly those focused on the wrist. Most datasets lack high-precision segmentation masks specifically annotated for the wrist region, and their corresponding BE scores are often incomplete or missing. This limits their suitability for RA-specific research, which requires high-quality, multi-dimensional annotated data. Therefore, the development of a wrist-focused CR dataset with detailed anatomical annotations and validated clinical scores is essential for the progress of intelligent RA imaging assessment.

3 Overview of Dataset

Ethical Considerations RAM-W600 dataset is in compliance with the guidelines of the Declaration of Helsinki and obtained approval from the Ethics Committee of Hokkaido University (approval number: 24-104) and Institute of Science Tokyo (approval number: A24672). All radiographs included in this dataset were collected with informed consent for research use and public release.

3.1 Image and Annotation

The dataset consisted of 621 hand posteroanterior projection (PA) radiographs from 154 patients with RA and 73 patients without RA. The images were obtained from three different institutions: Hokkaido Medical Center for Rheumatic Diseases (HMCRD) (Sapporo, Japan), Sapporo City General Hospital (SCGH) (Sapporo, Japan), Hokkaido University (HU) (Sapporo, Japan), and Digital Hand Atlas (DHA) from the University of Southern California (CA, US) [8]. Each institution has its own CR systems, and the dataset is managed using the digital imaging and communications in medicine (DICOM) standard, with the detailed information of imaging parameters referred to Table 6.

We employed specialized imaging processing methodologies to systematically construct wrist joint data. Initially, image cropping techniques were applied to focus on the wrist region, effectively eliminating interference from extraneous anatomical structures. Subsequent annotation procedures were conducted under the guidance of senior radiologists, comprising three principal components:

- **Anatomical Structure Annotation:** Precise contour delineation was performed for 14 wrist bones, including the first-fifth metacarpals (MC1-5), trapezium (Tr), trapezoid (Tz), scaphoid (Sca), lunate (Lu), capitate (Cap), hamate (Ham), pisiform & triquetrum (Tri), distal radius (Radius), and distal ulna (Ulna). A multi-label annotation strategy was implemented to independently mark each osseous structure.
- **Bone Location Annotation:** The SvdH BE scoring system focuses on five key joint regions: MC1, Tz, Sca, Lu, Radius, and Ulna. We performed ROI annotations on these areas.
- **SvdH BE Scoring Annotation:** BE assessment was conducted using the SvdH scoring system, specifically targeting five critical articular groups: MC1, Tz, Sca, Lu, Radius, and Ulna. This systematic evaluation focused on quantifying erosive changes at these predetermined anatomical sites.

With the division of these images, a comprehensive annotation pipeline was adopted, including professional annotators and strict inspection procedures. Further details of the data division and annotation can be found in Sec. B.

3.2 Statistics of RAM-W600

We present statistical analyses of the RAM-W600 dataset to characterize both the internal cohorts (HMCRD, SCGH, HU) and the external validation data (DHA). Key attributes, including patient demographics (age, gender), institutional sources, follow-up frequency (phase), and BE scores, were systematically examined. In addition, joint-specific BE score distributions were compared across anatomical locations. Detailed statistics are summarized in Fig. 2. The majority of patients in the internal cohort are female, with HMCRD contributing the largest number of cases and HU the fewest. Most wrist joints in this cohort are annotated with an SvdH BE score of 0, indicating minimal erosive changes, while non-zero scores remain relatively uncommon. In addition, most patients underwent

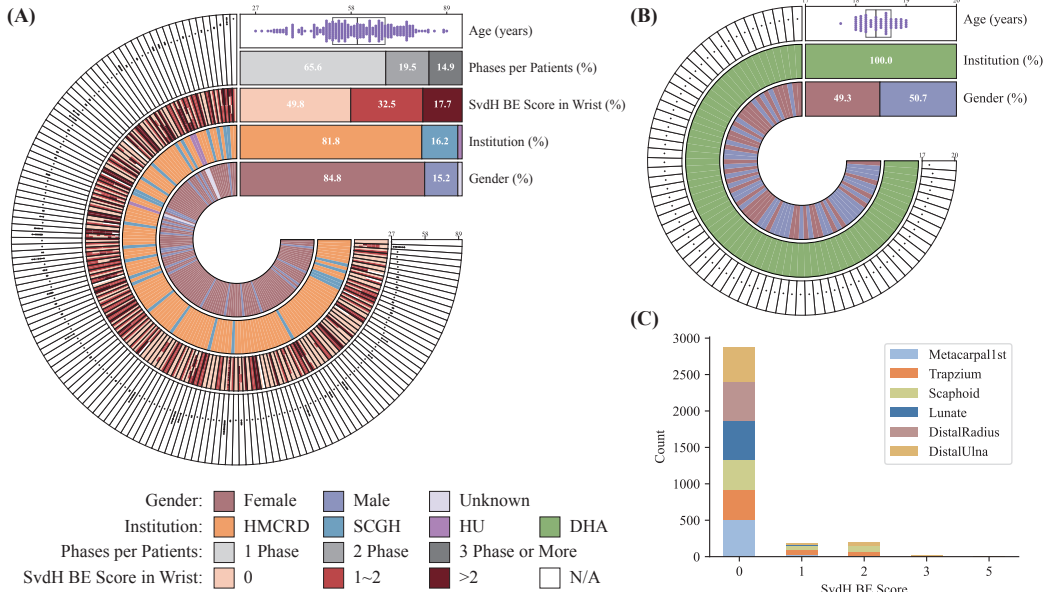


Figure 2: Distribution and Statistics for the age, gender, institution, number of shots, and BE scores in the RAM-W600 dataset. (A) Circular overview of the internal cohorts. Each bar around the circular plot represents a unique patient. The concentric layers from inner to outer encode: (i) Gender distribution. (ii) Institution distribution. (iii) SvdH BE scores in both wrists for each study. Patients with multiple studies are represented multiple times in this layer. (iv) The phase of imaging and the patient’s age at the time of each acquisition. (B) Circular overview of the external validation data. Similar to (A), each bar around the circular plot represents a unique patient. (C) Distribution of SvdH BE scores by joint surface.

only a single imaging phase, and the age distribution spans a broad range. In contrast, the external cohort (B) exhibits a balanced gender ratio and a narrow age distribution centered around 18 years, consistent with its role as a healthy control group. Joint-level SvdH BE annotations in (C) reveal a highly imbalanced distribution across joint surfaces, with the vast majority of joint faces assigned a score of 0. Higher scores, such as 3 or 5, are nearly absent.

4 Experiments and Benchmarks

4.1 Wrist Bone Segmentation

To evaluate wrist bone instance segmentation performance, we tested a series of widely used architectures and their variants on the RAM-W600 dataset, particularly those commonly adopted in medical images. The selected models included Unet [53], DeepLabV3 [10], FPN [37], PSPNet [74], DeepLabV3+[11], SegResNet[44], Unet++[75], SegFormer[70], TransUNet [9], UKAN [34], UMambaBot [39], UMambaEnc [39], SwinUMamba [38]. In line with standard practice, segmentation performance was quantified using Dice Similarity Coefficient (DSC) [13]; Normalized Surface Dice (NSD) [46]; Volumetric Overlap Error (VOE) [60]; Mean Surface Distance (MSD) [60]; and Relative Absolute Volume Difference (RAVD) [60]. The threshold for the NSD was set to 2 pixels.

Implementation details The dataset was split according to the configuration shown in Table 7 (a) in Sec. B.4. All experiments were conducted using a single RTX4090 GPU with a fixed seed of 3407 to ensure reproducibility. All radiographs were resized to 512×512 pixels and used as input to the model. Model training employed the AdamW optimizer with a weight decay of $1e-2$. The initial learning rate was set to $1e-4$ and decayed according to a cosine annealing schedule (CosineAnnealingLR). Training was carried out for 100 epochs using a batch size of 8 and standard data augmentation techniques.

Table 4: Instance segmentation results obtained on the Test set. The best results in each column are highlighted in **bold**, and the second-best values are underlined.

Model	DSC \uparrow			NSD \uparrow			VOE \downarrow	MSD \downarrow	RAVD \downarrow	Params	Time (ms)
	BE	nonBE	All	BE	nonBE	All					
Unet [53]	0.963	0.963	0.963	0.805	0.800	0.802	0.070	2.012	0.035	7.94M	13.570
DeepLabV3 [10]	0.964	0.967	0.966**	0.806	0.812	0.809	0.066	1.442	0.027	26.00M	9.190
FPN [37]	0.962	0.964	0.963**	0.776	0.781	0.778	0.071	1.544	0.032	23.15M	8.430
PSPNet [74]	0.949	0.951	0.950	0.669	0.663	0.666	0.095	2.174	0.043	21.49M	4.460
DeepLabV3+ [11]	0.965	0.968	0.967*	0.813	0.812	0.812	0.064	1.398	0.028	22.43M	5.570
SegResNet [44]	0.958	0.961	0.960	0.782	0.779	0.780	0.077	2.034	0.039	1.60M	4.930
Unet++ [75]	0.970	0.973	0.971**	0.850	0.862	0.856	0.055	1.243	0.027	2.41M	14.830
SegFormer [70]	0.966	0.968	0.967*	0.825	0.825	0.825	0.063	1.365	0.028	21.87M	5.040
TransUNet [9]	<u>0.974</u>	<u>0.976</u>	<u>0.975**</u>	<u>0.876</u>	<u>0.887</u>	<u>0.881</u>	<u>0.049</u>	<u>1.060</u>	<u>0.023</u>	105.91M	22.050
UKAN [34]	0.966	0.968	0.967**	0.816	0.821	0.818	0.063	1.383	0.029	6.36M	10.300
UMambaBot [39]	0.972	0.975	0.973**	0.867	0.881	0.874	0.051	1.147	0.024	4.42M	15.120
UMambaEnc [39]	0.972	<u>0.976</u>	0.974**	0.873	0.885	0.879	0.050	1.097	<u>0.023</u>	4.58M	16.440
SwinUMamba [38]	0.976	0.978	0.977**	0.893	0.906	0.900*	0.045	0.974	0.022	59.89M	38.520

Time: Inference time per image on RTX 4090 GPU.

Mann-Whitney U Test between BE & nonBE, *: $P < 0.05$; **: $P < 0.01$; ***: $P < 0.001$.

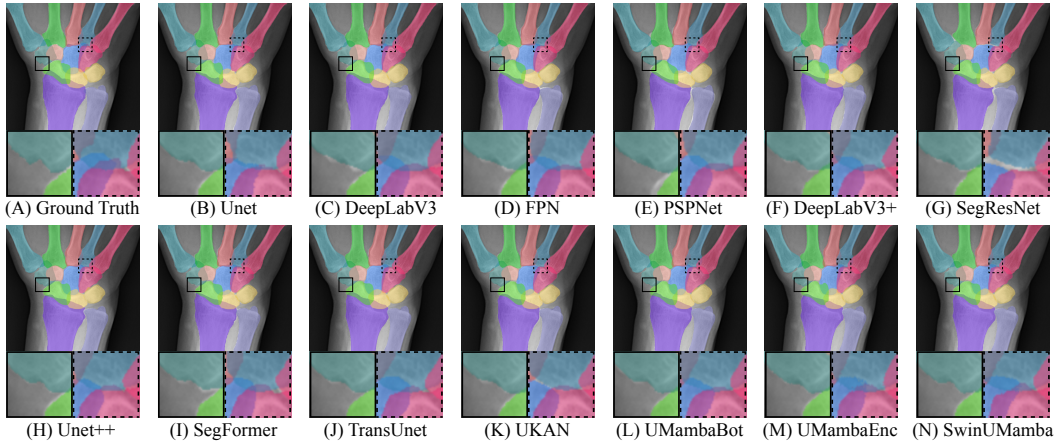


Figure 3: Wrist bone segmentation visualization results. The solid box indicates segmentation challenges caused by BE, while the dashed box represents difficulties arising from bone overlap.

Benchmark results The results shown in Table 4 demonstrate that mainstream models achieve outstanding performance in terms of DSC, with the highest value reaching 0.977 (SwinUMamba), indicating robust overlap accuracy in global segmentation regions. However, NSD values remain comparatively low (peak: 0.900), with significant variations across models, highlighting persistent challenges in bone boundary delineation. This limitation is closely tied to the inherent complexities of wrist bone segmentation: inter-bone occlusions leading to blurred boundaries, and BE regions characterized by abnormal texture and edge variations, which further exacerbate segmentation difficulty. Meanwhile, group analysis reveals statistically significant differences ($p < 0.05$ – 0.001) in DSC between BE and nonBE samples for most models, confirming the detrimental impact of BE on segmentation performance. In contrast, the NSD metric exhibited no statistically significant differences between groups. This discrepancy may stem from the heightened sensitivity of NSD to boundary errors and the larger variance in boundary-related discrepancies within the dataset, underscoring the intrinsic difficulty in handling bone edges. In conclusion, the primary bottleneck in this task lies in improving model robustness for complex bone boundaries.

Visualization Some representative results are shown in Fig. 3. Compared to the ground truth, mainstream networks exhibit performance degradation in segmenting bone edges with multi-layer occlusions, a challenge that becomes particularly pronounced under complex occlusion scenarios. Current models also demonstrate notable inconsistency, lacking reliable solutions to address this issue effectively. Furthermore, in the context of BE (RA), most existing architectures fail to adequately capture the inward collapse of bone edges caused by erosive changes. However, networks

Table 5: BE & nonBE classification results obtained on the Test set. The best results in each column are highlighted in **bold**, and the second-best values are underlined.

Model	BACC \uparrow	F1-Score \uparrow	DOR \uparrow	ACC \uparrow	SEN \uparrow	SPC \uparrow	PRE \uparrow	Params	Time(ms)
MobileViT [41]	<u>0.619</u>	<u>0.299</u>	3.238	0.771	<u>0.421</u>	0.817	0.232	4.94M	4.53
ResNet [23]	<u>0.597</u>	<u>0.279</u>	3.142	0.803	0.329	0.865	0.243	0.70M	1.99
MobileNet [29]	0.557	0.224	1.615	0.641	0.447	0.666	0.150	0.69M	1.72
LeViT [21]	0.560	0.218	<u>3.769</u>	0.858	0.171	0.948	0.302	7.01M	2.65
EfficientFormer [35]	0.548	0.207	1.771	0.766	0.263	0.832	0.171	3.25M	3.63
MedMamba [73]	0.622	0.314	3.841	<u>0.806</u>	0.382	0.862	<u>0.266</u>	14.45M	6.06
ConvKAN [6]	0.585	0.261	2.824	<u>0.801</u>	0.303	<u>0.867</u>	<u>0.230</u>	3.49M	29.96

Time: Inference time per image on RTX 4090 GPU.

incorporating Mamba-based architectures show partial improvements in handling such morphological distortions, as evidenced by comparative analyses. Visualization results further corroborate the persistent challenges in this segmentation task, primarily attributed to bone overlaps and erosion-induced structural anomalies. These factors collectively lead to fragmented or inaccurate edge predictions, emphasizing the need for dedicated architectural innovations.

Unlike natural images or other medical imaging modalities such as MRI and CT, conventional radiography captures the cumulative attenuation of X-rays along their path, resulting in grayscale representations of internal structures. This often leads to overlapping anatomical features and blurred boundaries in two-dimensional images. Moreover, pathological BE caused by RA can induce notable morphological changes in bone structure, further complicating segmentation. Traditional image processing and segmentation techniques often struggle to accurately delineate overlapping bone boundaries or detect morphological abnormalities resulting from pathological alterations. To address these challenges, future research may benefit from exploring multi-scale feature fusion strategies and advanced edge refinement techniques. Given the relatively fixed spatial arrangement of bones, incorporating global contextual information could be particularly advantageous for improving segmentation accuracy.

4.2 Classification of BE

The advanced binary classification methods of BE were evaluated on the RAM-W600 dataset. The selected classification models included MobileViT [41], ResNet [23], MobileNet [29], LeViT [21], EfficientFormer [35], MedMamba [73], and ConvKAN [6]. In line with standard practice, segmentation performance was quantified using balanced accuracy (BACC) [7], F1-score [12], diagnostic odds ratio (DOR) [20], accuracy (ACC) [19], sensitivity (SEN) [2], specificity (SPC) [2], and precision (PRE) [57].

Implementation details The dataset was split according to the configuration shown in Table 7 (b) in Sec. B.4. All experiments were conducted using a single RTX4090 GPU with a fixed random seed of 3407 to ensure reproducibility. All ROIs were resized to 224×224 pixels and used as input to the model. Model training utilized the AdamW optimizer with a weight decay of $1e-2$. The initial learning rate was set to $1e-6$ and decayed using a cosine annealing schedule (CosineAnnealingLR). Training was performed for 100 epochs with a batch size of 16 and standard data augmentation techniques.

Benchmark results The results in Table 5 reveal that mainstream models achieve only modest performance in terms of BACC and F1-score, with the best results reaching 0.622 and 0.314, respectively (MedMamba), indicating limited robustness in distinguishing BE from nonBE cases. In contrast, the DOR exhibits considerable variability across models, peaking at 3.841 (MedMamba). Notably, some models (e.g., LeViT) achieve high DOR values despite extremely low sensitivity, reflecting a bias toward negative predictions that artificially inflates the DOR. This inconsistency between BACC and DOR underscores the difficulty of the task, likely stemming from extreme class imbalance and the subtle radiographic presentation of BE. The confusion matrices in Fig. 4 provide a fine-grained view of each model’s classification behavior. All models display a clear asymmetry in performance between the majority class (nonBE) and the minority class (BE), further illustrating the inherent class imbalance and the challenge of detecting subtle BE features.

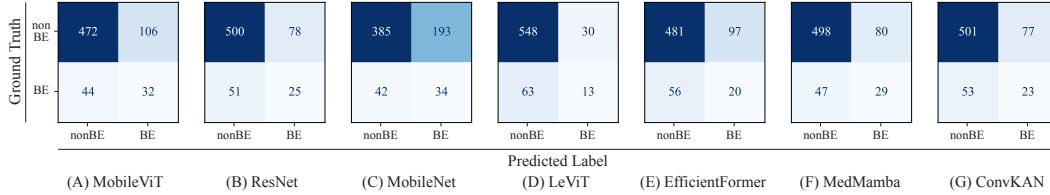


Figure 4: BE & nonBE confusion matrix results for classification of BE.

Future research should further focus on enhancing the model’s ability to detect subtle BE features under highly imbalanced data conditions. In clinical practice, early or mild BE lesions typically exhibit low visibility, presenting as small and inconspicuous regions that are easily confounded by overlapping bones, imaging artifacts, or noise. Although advanced BE lesions are more prominent in size, they often co-occur with other RA manifestations such as joint space narrowing and osteophyte formation, introducing additional sources of interference. These challenges collectively complicate the end-to-end scoring process for BE across different stages of the disease. To improve model performance on such difficult samples, future efforts may explore targeted augmentation strategies for minority classes or develop architectures capable of extracting weak pathological signals. Such advancements would enhance both the sensitivity and robustness of RA imaging assessment tools, thereby promoting their clinical applicability and translational value.

5 Conclusions and Limitations

We have introduced RAM-W600, the first publicly available multi-task conventional radiograph dataset for RA assessment, which encompasses two key tasks: wrist bone segmentation and SvdH BE localization and scoring. RAM-W600 has provided high-quality pixel-level annotations for the anatomically complex wrist region, which often presents with severe bone overlapping and erosive changes. In addition to detailed annotations, the dataset includes benchmark results for both segmentation and BE scoring tasks. Experimental findings have demonstrated the considerable challenges posed by these tasks, including the accurate delineation of bones in the presence of occlusion and erosion in the segmentation task, and the robust scoring of affected joints in the grading task. By establishing RAM-W600 and its associated benchmarks, we have offered a valuable resource for advancing research in medical image analysis. This dataset has opened new avenues for the development and validation of robust CAD systems and holds promise for improving diagnostic accuracy and clinical decision-making in the management of RA.

Despite its contributions to advancing CAD for RA, the RAM-W600 dataset has several limitations. First, the RA cases are primarily derived from a single geographic region and a relatively homogeneous ethnic population, which may limit the generalizability of models trained on the dataset to more diverse clinical settings. This lack of demographic variability could reduce the robustness of model performance across different populations. Second, the distribution of SvdH BE scores is imbalanced, with certain score levels notably underrepresented. This imbalance poses challenges for both training and evaluation, particularly in learning fine-grained disease severity and ensuring consistent performance across all stages of RA progression.

For wrist bone segmentation, future research should focus on developing dedicated network architectures that incorporate multi-scale contextual information and boundary-sensitive mechanisms. Such designs are essential to address the challenges posed by anatomical complexity and projection-induced overlap in wrist radiographs, particularly for achieving accurate delineation in regions affected by bone overlap and BE. Regarding the SvdH BE scoring task, early-stage lesions often present weak radiographic signals and are obscured by overlapping structures, while advanced-stage cases commonly exhibit coexisting RA-related features, resulting in complex local characteristics. In addition, the highly imbalanced distribution of BE samples continues to hinder lesion recognition in current approaches. To overcome these limitations, it is crucial to design model components capable of extracting subtle pathological features, thereby improving sensitivity and robustness in detecting early-stage BE. Advancements in these directions are expected to significantly enhance the automation of RA wrist image analysis and reinforce its clinical utility in diagnosis and longitudinal disease monitoring.

References

- [1] Daniel Aletaha and Josef S Smolen. Diagnosis and management of rheumatoid arthritis: a review. *Jama*, 320(13):1360–1372, 2018.
- [2] Douglas G Altman and J Martin Bland. Diagnostic tests. 1: Sensitivity and specificity. *BMJ: British Medical Journal*, 308(6943):1552, 1994.
- [3] Emran Mohammad Abu Anas, Abtin Rasouljan, Alexander Seitel, Kathryn Darras, David Wilson, Paul St John, David Pichora, Parvin Mousavi, Robert Rohling, and Purang Abolmaesumi. Automatic segmentation of wrist bones in ct using a statistical wrist shape + pose model. *IEEE transactions on medical imaging*, 35(8):1789–1801, 2016.
- [4] Anil K Bhat, Bhaskaranand Kumar, and Ashwath Acharya. Radiographic imaging of the wrist. *Indian journal of plastic surgery: official publication of the Association of Plastic Surgeons of India*, 44(2):186, 2011.
- [5] Zhiyan Bo, Laura C Coates, and Bartłomiej W Papież. Deep learning models to automate the scoring of hand radiographs for rheumatoid arthritis. In *Annual Conference on Medical Image Understanding and Analysis*, pages 398–413. Springer, 2024.
- [6] Alexander Dylan Bodner, Antonio Santiago Tepsich, Jack Natan Spolski, and Santiago Pourteau. Convolutional kolmogorov-arnold networks. *arXiv preprint arXiv:2406.13155*, 2024.
- [7] Kay Henning Brodersen, Cheng Soon Ong, Klaas Enno Stephan, and Joachim M Buhmann. The balanced accuracy and its posterior distribution. In *2010 20th international conference on pattern recognition*, pages 3121–3124. IEEE, 2010.
- [8] Fei Cao, HK Huang, Ewa Pietka, and Vicente Gilsanz. Digital hand atlas and web-based bone age assessment: system design and implementation. *Computerized medical imaging and graphics*, 24(5):297–307, 2000.
- [9] Jieneng Chen, Yongyi Lu, Qihang Yu, Xiangde Luo, Ehsan Adeli, Yan Wang, Le Lu, Alan L Yuille, and Yuyin Zhou. Transunet: Transformers make strong encoders for medical image segmentation. *arXiv preprint arXiv:2102.04306*, 2021.
- [10] Liang-Chieh Chen, George Papandreou, Florian Schroff, and Hartwig Adam. Rethinking atrous convolution for semantic image segmentation. *arXiv preprint arXiv:1706.05587*, 2017.
- [11] Liang-Chieh Chen, Yukun Zhu, George Papandreou, Florian Schroff, and Hartwig Adam. Encoder-decoder with atrous separable convolution for semantic image segmentation. In *Proceedings of the European conference on computer vision (ECCV)*, pages 801–818, 2018.
- [12] Nancy Chinchor and Beth M Sundheim. Muc-5 evaluation metrics. In *Fifth Message Understanding Conference (MUC-5): Proceedings of a Conference Held in Baltimore, Maryland, August 25-27, 1993*, 1993.
- [13] Lee R Dice. Measures of the amount of ecologic association between species. *Ecology*, 26(3):297–302, 1945.
- [14] Hongbo Du, Hai Wang, Chunlai Yang, Luyando Kabalata, Henian Li, and Changfu Qiang. Hand bone extraction and segmentation based on a convolutional neural network. *Biomedical Signal Processing and Control*, 89:105788, 2024.
- [15] Jörg Eschweiler, Jianzhang Li, Valentin Quack, Björn Rath, Alice Baroncini, Frank Hildebrand, and Filippo Migliorini. Anatomy, biomechanics, and loads of the wrist joint. *Life*, 12(2):188, 2022.
- [16] Fatemeh Ezzati and Parham Pezeshk. Radiographic findings of inflammatory arthritis and mimics in the hands. *Diagnostics*, 12(9):2134, 2022.
- [17] Lukas Folle, David Simon, Koray Tascilar, Gerhard Krönke, Anna-Maria Liphardt, Andreas Maier, Georg Schett, and Arnd Kleyer. Deep learning-based classification of inflammatory arthritis by identification of joint shape patterns—how neural networks can tell us where to “deep dive” clinically. *Frontiers in Medicine*, 9:850552, 2022.

- [18] Brent Foster, Anand A Joshi, Marissa Borgese, Yasser Abdelhafez, Robert D Boutin, and Abhijit J Chaudhari. Wrist: A wrist image segmentation toolkit for carpal bone delineation from mri. *Computerized Medical Imaging and Graphics*, 63:31–40, 2018.
- [19] Jerome Friedman. The elements of statistical learning: Data mining, inference, and prediction. (*No Title*), 2009.
- [20] Afina S Glas, Jeroen G Lijmer, Martin H Prins, Gouke J Bonsel, and Patrick MM Bossuyt. The diagnostic odds ratio: a single indicator of test performance. *Journal of clinical epidemiology*, 56(11):1129–1135, 2003.
- [21] Benjamin Graham, Alaaeldin El-Nouby, Hugo Touvron, Pierre Stock, Armand Joulin, Hervé Jégou, and Matthijs Douze. Levit: a vision transformer in convnet’s clothing for faster inference. In *Proceedings of the IEEE/CVF international conference on computer vision*, pages 12259–12269, 2021.
- [22] Safwan S Halabi, Luciano M Prevedello, Jayashree Kalpathy-Cramer, Artem B Mamonov, Alexander Bilbily, Mark Cicero, Ian Pan, Lucas Araújo Pereira, Rafael Teixeira Sousa, Nitamar Abdala, et al. The rsna pediatric bone age machine learning challenge. *Radiology*, 290(2):498–503, 2019.
- [23] Kaiming He, Xiangyu Zhang, Shaoqing Ren, and Jian Sun. Deep residual learning for image recognition. In *Proceedings of the IEEE conference on computer vision and pattern recognition*, pages 770–778, 2016.
- [24] Yuri Hioki, Koji Makino, Kensuke Koyama, Hiroataka Haro, and Hidetsugu Terada. Evaluation method of rheumatoid arthritis by the x-ray photograph using deep learning. In *2021 IEEE 3rd Global Conference on Life Sciences and Technologies (LifeTech)*, pages 444–447. IEEE, 2021.
- [25] T Hirano, M Nishide, N Nonaka, J Seita, K Ebina, K Sakurada, et al. Development and validation of a deep-learning model for scoring of radiographic finger joint destruction in rheumatoid arthritis. *rheumatol adv pract*. 2019. available from:; 3.
- [26] Toru Hirano, Masayuki Nishide, Naoki Nonaka, Jun Seita, Kosuke Ebina, Kazuhiro Sakurada, and Atsushi Kumanogoh. Development and validation of a deep-learning model for scoring of radiographic finger joint destruction in rheumatoid arthritis. *Rheumatology advances in practice*, 3(2):rkz047, 2019.
- [27] Stefanie Hirsiger, Andreas Schweizer, Junichi Miyake, Ladislav Nagy, and Philipp Fürnstahl. Corrective osteotomies of phalangeal and metacarpal malunions using patient-specific guides: Ct-based evaluation of the reduction accuracy. *Hand*, 13(6):627–636, 2018.
- [28] Jan Lucas Hoving, Rachele Buchbinder, Stephen Hall, Gary Lawler, Peter Coombs, Stephen McNealy, Paul Bird, and David Connell. A comparison of magnetic resonance imaging, sonography, and radiography of the hand in patients with early rheumatoid arthritis. *The Journal of rheumatology*, 31(4):663–675, 2004.
- [29] Andrew G Howard. Mobilenets: Efficient convolutional neural networks for mobile vision applications. *arXiv preprint arXiv:1704.04861*, 2017.
- [30] Yinghe Huo, Koen L Vincken, Desiree Van Der Heijde, Maria JH De Hair, Floris P Lafeber, and Max A Viergever. Automatic quantification of radiographic wrist joint space width of patients with rheumatoid arthritis. *IEEE Transactions on Biomedical Engineering*, 64(11):2695–2703, 2017.
- [31] Bo-kyeong Kang, Yelin Han, Jaehoon Oh, Jongwoo Lim, Jongbin Ryu, Myeong Seong Yoon, Juncheol Lee, and Soorack Ryu. Automatic segmentation for favourable delineation of ten wrist bones on wrist radiographs using convolutional neural network. *Journal of Personalized Medicine*, 12(5):776, 2022.
- [32] Kathryn M Kingsmore, Christopher E Puglisi, Amrie C Grammer, and Peter E Lipsky. An introduction to machine learning and analysis of its use in rheumatic diseases. *Nature Reviews Rheumatology*, 17(12):710–730, 2021.

- [33] Hyungeun Lee, Ung Hwang, Seungwon Yu, Chang-Hun Lee, and Kijung Yoon. Osteoporosis prediction from hand and wrist x-rays using image segmentation and self-supervised learning. *arXiv preprint arXiv:2311.06834*, 2023.
- [34] Chenxin Li, Xinyu Liu, Wuyang Li, Cheng Wang, Hengyu Liu, Yifan Liu, Zhen Chen, and Yixuan Yuan. U-kan makes strong backbone for medical image segmentation and generation. In *Proceedings of the AAAI Conference on Artificial Intelligence*, volume 39, pages 4652–4660, 2025.
- [35] Yanyu Li, Geng Yuan, Yang Wen, Ju Hu, Georgios Evangelidis, Sergey Tulyakov, Yanzhi Wang, and Jian Ren. Efficientformer: Vision transformers at mobilenet speed. *Advances in Neural Information Processing Systems*, 35:12934–12949, 2022.
- [36] Chung-Yueh Lien, Hao-Jan Wang, Cheng-Kai Lu, Tzu-Hsuan Hsu, Woei-Chyn Chu, and Chien-Chih Lai. Deep learning with an attention mechanism for enhancing automated modified total sharp/van der heijde scoring of hand x-ray images in rheumatoid arthritis. *Journal of Medical and Biological Engineering*, pages 1–9, 2025.
- [37] Tsung-Yi Lin, Piotr Dollár, Ross Girshick, Kaiming He, Bharath Hariharan, and Serge Belongie. Feature pyramid networks for object detection. In *Proceedings of the IEEE conference on computer vision and pattern recognition*, pages 2117–2125, 2017.
- [38] Jiarun Liu, Hao Yang, Hong-Yu Zhou, Yan Xi, Lequan Yu, Cheng Li, Yong Liang, Guangming Shi, Yizhou Yu, Shaoting Zhang, et al. Swin-umamba: Mamba-based unet with imagenet-based pretraining. In *International Conference on Medical Image Computing and Computer-Assisted Intervention*, pages 615–625. Springer, 2024.
- [39] Jun Ma, Feifei Li, and Bo Wang. U-mamba: Enhancing long-range dependency for biomedical image segmentation. *arXiv preprint arXiv:2401.04722*, 2024.
- [40] Krzysztof Maziarz, Anna Krason, and Zbigniew Wojna. Deep learning for rheumatoid arthritis: Joint detection and damage scoring in x-rays. *arXiv preprint arXiv:2104.13915*, 2021.
- [41] Sachin Mehta and Mohammad Rastegari. Mobilevit: light-weight, general-purpose, and mobile-friendly vision transformer. *arXiv preprint arXiv:2110.02178*, 2021.
- [42] Kazuki Miyama, Ryoma Bise, Satoshi Ikemura, Kazuhiro Kai, Masaya Kanahori, Shinkichi Arisumi, Taisuke Uchida, Yasuharu Nakashima, and Seiichi Uchida. Deep learning-based automatic-bone-destruction-evaluation system using contextual information from other joints. *Arthritis Research & Therapy*, 24(1):227, 2022.
- [43] Douglas C Moore, Joseph J Crisco, Theodore G Trafton, and Evan L Leventhal. A digital database of wrist bone anatomy and carpal kinematics. *Journal of biomechanics*, 40(11):2537–2542, 2007.
- [44] Andriy Myronenko. 3d mri brain tumor segmentation using autoencoder regularization. In *International MICCAI brainlesion workshop*, pages 311–320. Springer, 2018.
- [45] Arjun Nanduri, Alison Kim, Carolyn Nolan, Jesse Dubey, and Andrew Barbera. Triquetrum fracture with pisiform dislocation. *Orthopedic Reviews*, 14(2):32339, 2022.
- [46] Stanislav Nikolov, Sam Blackwell, Alexei Zverovitch, Ruheena Mendes, Michelle Livne, Jeffrey De Fauw, Yojan Patel, Clemens Meyer, Harry Askham, Bernardino Romera-Paredes, et al. Clinically applicable segmentation of head and neck anatomy for radiotherapy: deep learning algorithm development and validation study. *Journal of medical Internet research*, 23(7):e26151, 2021.
- [47] Yafei Ou, Prasoon Ambalathankandy, Ryunosuke Furuya, Seiya Kawada, Tianyu Zeng, Yujie An, Tamotsu Kamishima, Kenichi Tamura, and Masayuki Ikebe. A sub-pixel accurate quantification of joint space narrowing progression in rheumatoid arthritis. *IEEE Journal of Biomedical and Health Informatics*, 27(1):53–64, 2023.

- [48] Benjamin Schultz Overgaard, Anders Bossel Holst Christensen, Lene Terslev, Thiusius Rajeeth Savarimuthu, and Søren Andreas Just. Artificial intelligence model for segmentation and severity scoring of osteophytes in hand osteoarthritis on ultrasound images. *Frontiers in Medicine*, 11:1297088, 2024.
- [49] Raj Ponnusamy, Ming Zhang, Zhiheng Chang, Yue Wang, Carmine Guida, Samantha Kuang, Xinyue Sun, Jordan Blackadar, Jeffrey B Driban, Timothy McAlindon, et al. Automatic measuring of finger joint space width on hand radiograph using deep learning and conventional computer vision methods. *Biomedical signal processing and control*, 84:104713, 2023.
- [50] Karl Ludger Radke, Lena Marie Wollschläger, Sven Nebelung, Daniel Benjamin Abrar, Christoph Schleich, Matthias Boschheidgen, Miriam Frenken, Justus Schock, Dirk Klee, Jens Frahm, et al. Deep learning-based post-processing of real-time mri to assess and quantify dynamic wrist movement in health and disease. *Diagnostics*, 11(6):1077, 2021.
- [51] Stefan Raith, Matthias Deitermann, Tobias Pankert, Jianzhang Li, Ali Modabber, Frank Hölzle, Frank Hildebrand, and Jörg Eschweiler. Multi-label segmentation of carpal bones in mri using expansion transfer learning. *Physics in Medicine and Biology*, 2025.
- [52] Eric EJ Raven, Michel PJ van den Bekerom, Annechien Beumer, and C Niek van Dijk. Radiocarpal and midcarpal instability in rheumatoid patients: a systematic review. *The Open Orthopaedics Journal*, 9:246, 2015.
- [53] Olaf Ronneberger, Philipp Fischer, and Thomas Brox. U-net: Convolutional networks for biomedical image segmentation. In *Medical image computing and computer-assisted intervention—MICCAI 2015: 18th international conference, Munich, Germany, October 5-9, 2015, proceedings, part III 18*, pages 234–241. Springer, 2015.
- [54] Maja Schlereth, Melek Yalcin Mutlu, Jonas Utz, Sara Bayat, Tobias Heimann, Jingna Qiu, Chris Ehring, Chang Liu, Michael Uder, Arnd Kleyer, et al. Deep learning-based classification of erosion, synovitis and osteitis in hand mri of patients with inflammatory arthritis. *RMD open*, 10(2):e004273, 2024.
- [55] Ronnie Sebro and Cynthia De la Garza-Ramos. Machine learning for opportunistic screening for osteoporosis from ct scans of the wrist and forearm. *Diagnostics*, 12(3):691, 2022.
- [56] Kassem Sharif, Alaa Sharif, Fareed Jumah, Rod Oskouian, and R Shane Tubbs. Rheumatoid arthritis in review: Clinical, anatomical, cellular and molecular points of view. *Clinical Anatomy*, 31(2):216–223, 2018.
- [57] Marina Sokolova and Guy Lapalme. A systematic analysis of performance measures for classification tasks. *Information processing & management*, 45(4):427–437, 2009.
- [58] Berend C Stoel, Marius Staring, Monique Reijniere, and Annette HM van der Helm-van Mil. Deep learning in rheumatological image interpretation. *Nature Reviews Rheumatology*, 20(3):182–195, 2024.
- [59] Dongmei Sun, Thanh M Nguyen, Robert J Allaway, Jelai Wang, Verena Chung, Thomas V Yu, Michael Mason, Isaac Dimitrovsky, Lars Ericson, Hongyang Li, et al. A crowdsourcing approach to develop machine learning models to quantify radiographic joint damage in rheumatoid arthritis. *JAMA network open*, 5(8):e2227423–e2227423, 2022.
- [60] Abdel Aziz Taha and Allan Hanbury. Metrics for evaluating 3d medical image segmentation: analysis, selection, and tool. *BMC medical imaging*, 15:1–28, 2015.
- [61] Bachir Taouli, Souhil Zaim, Charles G Peterfy, John A Lynch, Alexander Stork, Ali Guermazi, Bo Fan, Kenneth H Fye, and Harry K Genant. Rheumatoid arthritis of the hand and wrist: comparison of three imaging techniques. *American Journal of Roentgenology*, 182(4):937–943, 2004.
- [62] EHS Teule, N Lessmann, EPA van der Heijden, and S Hummelink. Automatic segmentation and labelling of wrist bones in four-dimensional computed tomography datasets via deep learning. *Journal of Hand Surgery (European Volume)*, 49(4):507–509, 2024.

- [63] Kemal Üreten, Hasan Erbay, and Hadi Hakan Maraş. Detection of rheumatoid arthritis from hand radiographs using a convolutional neural network. *Clinical rheumatology*, 39:969–974, 2020.
- [64] DMFM Van der Heijde. How to read radiographs according to the sharp/van der heijde method. *The Journal of rheumatology*, 27(1):261–263, 2000.
- [65] DMFM Van der Heijde, T Dankert, F Nieman, R Rau, and M Boers. Reliability and sensitivity to change of a simplification of the sharp/van der heijde radiological assessment in rheumatoid arthritis. *Rheumatology*, 38(10):941–947, 1999.
- [66] Hao-Jan Wang, Chi-Ping Su, Chien-Chih Lai, Wun-Rong Chen, Chi Chen, Liang-Ying Ho, Woei-Chyn Chu, and Chung-Yueh Lien. Deep learning-based computer-aided diagnosis of rheumatoid arthritis with hand x-ray images conforming to modified total sharp/van der heijde score. *Biomedicines*, 10(6):1355, 2022.
- [67] Haolin Wang, Yafei Ou, Prasoon Ambalathankandy, Gen Ota, Pengyu Dai, Masayuki Ikebe, Kenji Suzuki, and Tamotsu Kamishima. Bls-gan: A deep layer separation framework for eliminating bone overlap in conventional radiographs. In *Proceedings of the AAAI Conference on Artificial Intelligence*, volume 39, pages 7674–7681, 2025.
- [68] Haolin Wang, Yafei Ou, Prasoon Ambalathankandy, Gen Ota, Pengyu Dai, Masayuki Ikebe, Kenji Suzuki, and Tamotsu Kamishima. Layer separation: Adjustable joint space width images synthesis in conventional radiography. *arXiv preprint arXiv:2502.01972*, 2025.
- [69] Haolin Wang, Yafei Ou, Wanxuan Fang, Prasoon Ambalathankandy, Naoto Goto, Gen Ota, Taichi Okino, Jun Fukae, Kenneth Sutherland, Masayuki Ikebe, et al. A deep registration method for accurate quantification of joint space narrowing progression in rheumatoid arthritis. *Computerized Medical Imaging and Graphics*, 108:102273, 2023.
- [70] Enze Xie, Wenhai Wang, Zhiding Yu, Anima Anandkumar, Jose M Alvarez, and Ping Luo. Segformer: Simple and efficient design for semantic segmentation with transformers. *Advances in neural information processing systems*, 34:12077–12090, 2021.
- [71] Fan Yang, Xin Weng, Yuehong Miao, Yuhui Wu, Hong Xie, and Pinggui Lei. Deep learning approach for automatic segmentation of ulna and radius in dual-energy x-ray imaging. *Insights into Imaging*, 12:1–9, 2021.
- [72] Chungwun Yiu, James Francis Griffith, Fan Xiao, Lin Shi, Bingjing Zhou, Su Wu, and Lai-Shan Tam. Automated quantification of wrist bone marrow oedema, pre-and post-treatment, in early rheumatoid arthritis. *Rheumatology Advances in Practice*, 8(3):rkae073, 2024.
- [73] Yubiao Yue and Zhenzhang Li. Medmamba: Vision mamba for medical image classification. *arXiv preprint arXiv:2403.03849*, 2024.
- [74] Hengshuang Zhao, Jianping Shi, Xiaojuan Qi, Xiaogang Wang, and Jiaya Jia. Pyramid scene parsing network. In *Proceedings of the IEEE conference on computer vision and pattern recognition*, pages 2881–2890, 2017.
- [75] Zongwei Zhou, Md Mahfuzur Rahman Siddiquee, Nima Tajbakhsh, and Jianming Liang. Unet++: A nested u-net architecture for medical image segmentation. In *Deep learning in medical image analysis and multimodal learning for clinical decision support: 4th international workshop, DLMIA 2018, and 8th international workshop, ML-CDS 2018, held in conjunction with MICCAI 2018, Granada, Spain, September 20, 2018, proceedings 4*, pages 3–11. Springer, 2018.

A RAM-W600 Data Access and Format

The data can be accessed on HuggingFace at <https://huggingface.co/datasets/TokyoTechMagicYang/ram-w600>. The dataset has a permanent DOI: <https://doi.org/10.57967/hf/5328>. The benchmark and code can be accessed on Github at <https://github.com/YSongxiao/ram-w600>.

The dataset is organised in two main folders (Segmentation/ and BE_SvdH_Prediction/) corresponding to two tasks. The dataset structure is shown as follows:

```
RAM-W600/
|-- BoneLocationDetection/
|   |-- images/                # Contains all input images in BMP format
|       |-- 0145_0004_L.bmp
|       |-- 0145_0004_R.bmp
|       |-- ...
|   |-- Joints.coco.json      # Ground-truth annotations for joints'
|   ↳ locations
|-- BoneSegmentation/
|   |-- images/                # Contains all input images in BMP
|   ↳ format
|       |-- 0001_0001_L.bmp
|       |-- 0001_0001_R.bmp
|       |-- ...
|   |-- masks/                # Contains corresponding masks in
|   ↳ NumPy (.numpy) format
|       |-- train/
|           |-- 0006_0001_L.npy
|           |-- ...
|           |-- val/
|               |-- 0001_0001_R.npy
|               |-- ...
|           |-- test/
|               |-- 0002_0001_L.npy
|               |-- ...
|-- SvdHBEScoreClassification/
|   |-- train/
|       |-- 0003_0001_L/
|           |-- DistalRadius.bmp
|           |-- DistalUlna.bmp
|           |-- ...
|       |-- ...
|   |-- val/
|       |-- 0001_0001_R/
|           |-- DistalRadius.bmp
|           |-- DistalUlna.bmp
|           |-- ...
|       |-- ...
|   |-- test/
|       |-- 0005_0001_L/
|           |-- DistalRadius.bmp
|           |-- DistalUlna.bmp
|           |-- ...
|       |-- ...
|   |-- JointBE_SvdH_GT.json  # Ground-truth annotations for joint
|   ↳ BE scores
```

- BoneSegmentation/images/: Contains all original images in BMP format. Each file is named as [PatientID]_[StudyID]_[L/R].bmp, where L and R indicate the left or right hand, respectively.
- BoneSegmentation/masks/: Contains the corresponding segmentation masks stored as NumPy arrays (.npy). The masks are organized into train/, val/, and test/ subsets, with filenames matching the corresponding images.

- JointLocationDetection/images/: Contains all original images in BMP format. Each file is named as [PatientID]_[StudyID]_[L/R].bmp, where L and R indicate the left or right hand, respectively.
- JointLocationDetection/Joints.coco.json: A JSON file containing ground-truth annotations for the joint scores, indexed by case identifiers. The format of entries in JSON file is shown as follows:

```
{
  "images": [
    {
      "id": 0,
      "file_name": "0334_0001_R.bmp",
      "width": 600,
      "height": 600
    },
    ...
  ],
  "annotations": [
    {
      "id": 3281,
      "image_id": 546,
      "category_id": 1,
      "bbox": [170.0, 305.88, 235, 235],
      "area": 23680.95,
      "segmentation": [],
      "iscrowd": 0
    },
    ...
  ],
  "categories": [
    {
      "id": 1,
      "name": "DistalRadius",
      "supercategory": "joint"
    },
    {
      "id": 2,
      "name": "DistalUlna",
      "supercategory": "joint"
    },
    ...
  ]
}
```

Each entry in the images list represents a wrist radiograph, while the annotations list contains bounding box annotations for individual joints, identified by their category_id. The categories section maps category IDs to specific joint names such as Lunate, Scaphoid, and Trapezium.

- SvdHBEScoreClassification/train/val/test/: Each subset contains folders named as [PatientID]_[StudyID]_[L/R], representing individual cases. Inside each folder are six ROI images in BMP format, each corresponding to different joint surfaces.
- SvdHBEScoreClassification/JointBE_SvdH_GT.json: A JSON file containing ground-truth annotations for the joint scores, indexed by case identifiers. The format of entries in JSON file is shown as follows:

```
{
  "identifier": "0035_0001_L",
  "patient_id": "0035",
  "study_id": "0001",
  "hand": "L",
  "joints": {
    "Metacarpal1st": 0,
    "Trapezium": 0,

```

```

    "Scaphoid": 0,
    "Lunate": 0,
    "DistalRadius": 0,
    "DistalUlna": 0
  }
}

```

B Detailed Information of RAM-W600

B.1 License and Attribution

The conventional radiographs and associated annotations (segmentation masks and SvdH BE scores) in the dataset are licensed under the Creative Commons Attribution 4.0 International License (CC BY 4.0).

For proper attribution when using this dataset in any publications or research outputs, please cite with the DOI.

Suggested Citation: Yang, S., Wang, H., Fu, Y., Tian, Y., Kamishima, T., Ikebe, M., Ou, Y., & Okutomi, M.(2025). RAM-W600: A Multi-Task Wrist Dataset and Benchmark for Rheumatoid Arthritis. <https://doi.org/10.57967/hf/5328>

B.2 Data Rights Compliance and Issue Reporting

We are committed to complying data protection rights in accordance with relevant regulations, including but not limited to the General Data Protection Regulation (GDPR). All personally identifiable information (PII) has been removed through anonymization techniques. If any individual represented in the dataset wishes to have their data removed, we provide a clear and accessible process for issue reporting and resolution via our GitHub repository. Concerned parties are encouraged to contact the authors directly through the contact form linked on the GitHub page. Upon receiving a request, we will engage with the individual to verify their identity and promptly remove the relevant data entries from the dataset.

B.3 Data Acquisition

Radiographs were collected from four institutions with varying imaging configurations, including differences in equipment models, acquisition settings, and image resolutions, as shown in Table 6.

Table 6: Radiographic imaging configuration parameters

	HU	HMCRD	SCGH	DHA
Model	-	Radnext 32	KXO-50G	IPI LAB(Secondary)
Manufacturer	FUJIFILM	HITACHI	TOSHIBA	Array(Secondary)
Aluminum filter (mm)	NO	0.5	NO	-
Tube voltage (kV)	-	50	45	-
Tube current (mA)	-	100	250	-
Exposure time (mSec)	-	25	14	-
Source to image (cm)	-	100	100	-
Resolution (mm/pixel)	0.15	0.15	0.15	-
Image size (pixel)	2010×1670	2010×1490	2010×1490	1744×2126
Bit depth (bit)	16	10	10	16

HU: Faculty of Health Sciences, Hokkaido University.

HMCRD: Hokkaido Medical Center for Rheumatic Diseases, Japan.

SCGH: Sapporo City General Hospital, Japan.

DHA: Digital Hand Atlas, University of Southern California, US.

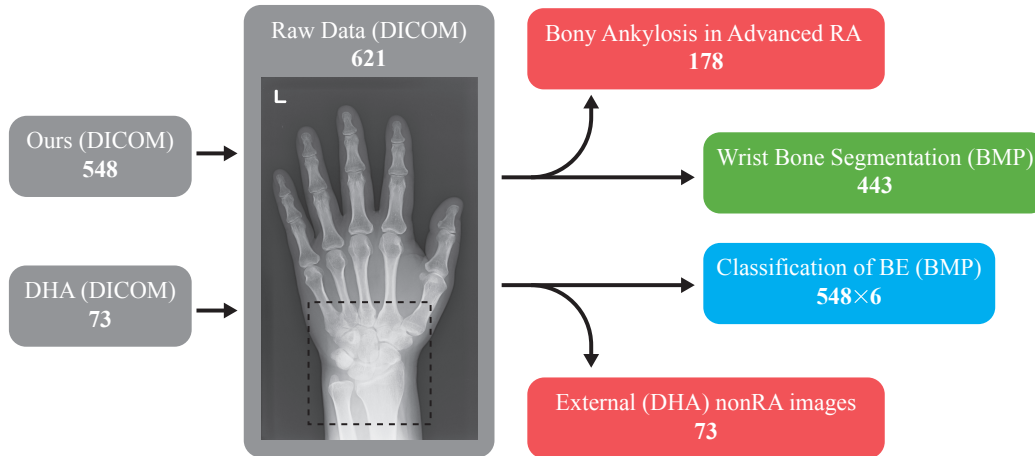


Figure 5: Data filtering process for RA dataset construction. A total of 621 DICOM-format wrist radiographs were collected, including 548 from our institution and 73 external non-RA images from DHA. After filtering, 251 cases with advanced RA showing bony ankylosis were excluded. The remaining images were used for two primary tasks: wrist bone instance segmentation (443 BMP images) and BE classification (548 images \times 6 joint areas). The 73 external DHA images were used only for non-RA comparison purposes.

B.4 Data Pre-Processing

In the pre-processing pipeline of RAM-W600 (Fig. 5), we first localize the ROI around the wrist across all 621 DICOM-format hand radiographs. For the wrist bone segmentation task, we exclude 251 images exhibiting bony ankylosis associated with advanced RA, resulting in a curated subset of 443 BMP-format images for segmentation. For the BE classification task, we exclude only 73 non-RA images from the external DHA dataset, retaining all 548 RA cases from our internal dataset. These cases are subsequently converted to BMP format, and six joint-level crops are extracted per image, yielding a total of 3288 samples for BE classification.

The wrist bone segmentation dataset and the SvdH BE scoring dataset are split independently. To prevent data leakage and reduce potential bias, we randomly partition the cases into training, validation, and test sets based on unique patient IDs using an approximate ratio of 70%/10%/20%. Table 7 summarizes the distribution of the six wrist joints (1st Metacarpal, Trapezium, Scaphoid, Lunate, Radius, and Ulna) across scores 0–5 within the training, validation, and test subsets of both datasets. The majority of joints are assigned an SvdH BE score of 0, while those with a score of 5 are extremely rare. In both tasks, the number of joints decreases as the score increases, resulting in a clearly imbalanced distribution.

B.5 Dataset Maintenance

As the authors and maintainers of this dataset, we affirm that while the dataset is self-contained and does not depend on any external links or content, we may provide future updates, such as adding new cases or incorporating additional tasks. These potential updates aim to enhance the dataset’s value while maintaining its long-term usability.

B.6 Wrist Bone Segmentation

Wrist bone segmentation from radiographs is a critical prerequisite for downstream tasks such as joint localization, morphological analysis, and BE scoring in RA assessment. As illustrated in Fig. 6, this task involves delineating multiple overlapping and irregularly shaped carpal and metacarpal bones, which often exhibit low contrast and anatomical ambiguity in radiographs. Accurate segmentation enables reliable quantification of structural features and supports automated interpretation in clinical workflows.

Table 7: Joint score distribution across train, valid, and test sets of RAM-W600.

(a) <i>Wrist Bone Segmentation</i> Dataset							(b) <i>SvdH BE Scoring</i> Dataset						
Score	MC 1	Tr	Sca	Lu	Radius	Ulna	Score	MC 1	Tr	Sca	Lu	Radius	Ulna
<i>Train Set</i>							<i>Train Set</i>						
0	299	268	264	307	304	278	0	350	291	289	374	375	323
1	4	10	13	0	3	8	1	23	48	36	3	4	15
2	6	28	29	2	2	23	2	10	39	46	4	4	40
3	0	3	3	0	0	0	3	0	5	10	0	0	3
5	0	0	0	0	0	0	5	0	0	2	2	0	2
<i>Valid Set</i>							<i>Valid Set</i>						
0	41	38	35	41	42	38	0	51	41	37	53	53	54
1	2	1	0	1	1	2	1	4	7	7	3	1	0
2	1	5	7	2	1	4	2	1	7	11	0	2	1
3	0	0	2	0	0	0	3	0	1	1	0	0	0
5	0	0	0	0	0	0	5	0	0	0	0	0	1
<i>Test Set</i>							<i>Test Set</i>						
0	82	74	65	88	88	84	0	106	82	81	105	105	99
1	4	4	7	2	0	1	1	2	13	12	2	4	1
2	4	10	16	0	2	4	2	1	14	16	2	0	7
3	0	2	2	0	0	1	3	0	0	0	0	0	2
5	0	0	0	0	0	0	5	0	0	0	0	0	0

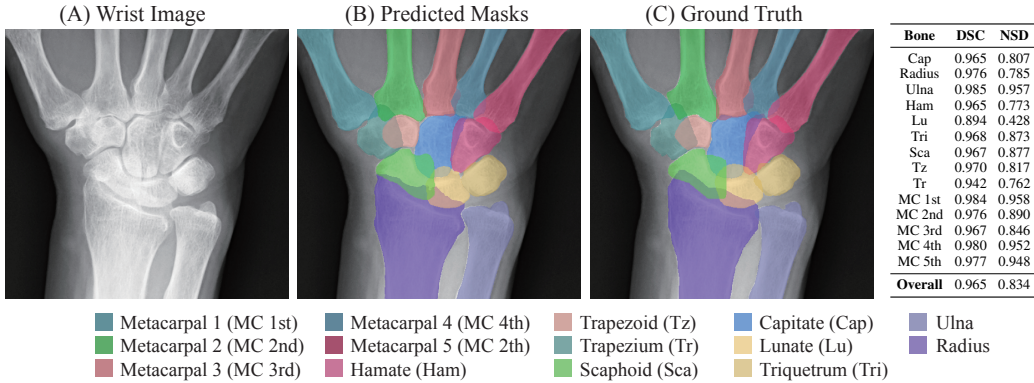


Figure 6: Wrist bone segmentation. (A) Original wrist radiograph. (B) Predicted instance segmentation masks. (C) Ground truth annotations. The right panel reports the segmentation performance per bone.

In this task, we annotate 14 distinct wrist bones, including both carpal, metacarpal components and Radius & Ulna. Notably, the pisiform and triquetrum bones are difficult to distinguish in clinical practice due to their overlapping appearance and low visibility on standard radiographs. Consequently, it is challenging to evaluate them as independent diagnostic regions [45]. Therefore, we merge these two structures into a single category during annotation to reflect their practical indistinguishability. The input to the segmentation model is the wrist ROI cropped from the radiograph, and the output and ground truth are a pixel-wise mask for each annotated bone, as illustrated in Fig. 7.

B.7 Classification of BE

BE classification is a key component of the SvdH scoring system, widely adopted in clinical practice for evaluating joint damage in RA. As illustrated in Fig. 8, this task involves identifying subtle pathological changes in individual carpal bones from radiographs, such as cortical breaks and irregular bone surfaces. The classification task is particularly challenging due to the subtlety of erosion features and the high degree of anatomical overlap in wrist joints. Accurate BE detection is essential for automated RA scoring systems and downstream severity assessment, yet remains difficult for both traditional and deep learning models, especially under class imbalance and in early-stage lesions.

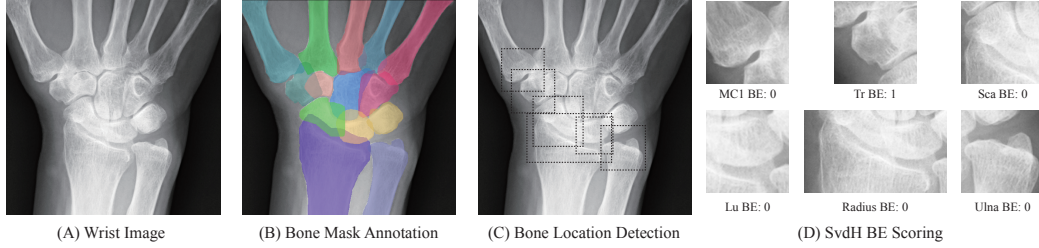


Figure 7: Image input and annotation. (A) Raw wrist radiograph. (B) Instance bone segmentation mask annotation (C) bone location annotations for target regions. (D) SvdH BE scores assigned to each joint region.

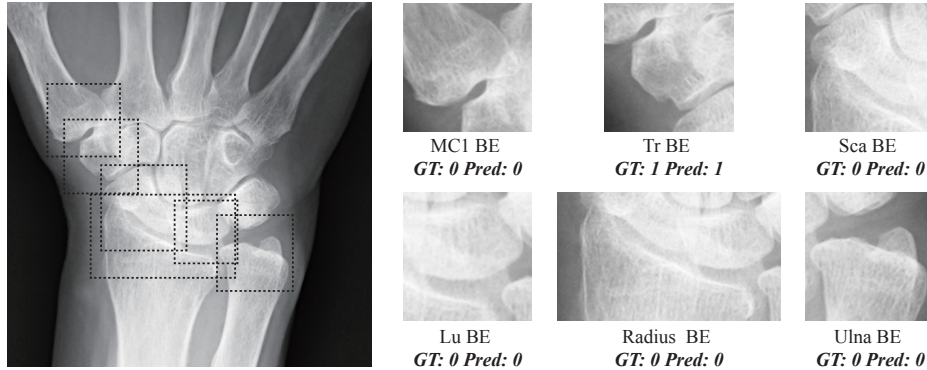


Figure 8: BE and nonBE Classification. The left panel shows six annotated joint regions used for BE classification. The right panels display each joint with ground truth (GT) and predicted (Pred) SvdH BE scores.

In this task, we annotate the SvdH BE scores for six joint surfaces within the wrist. To formulate the problem as a binary classification task, all joint surfaces with non-zero scores were treated as positive cases (i.e., exhibiting BE), while those with a score of zero were treated as negative cases (i.e., without BE). The input to the model is the ROI corresponding to an individual joint surface, and the output is a probability distribution over the two classes, representing the model’s confidence in the presence or absence of BE, as shown in Fig. 7.

C Detailed Analysis of Experimental Results

C.1 Wrist Bone Segmentation

Table 8 and Table 9 demonstrate that all models achieve strong segmentation performance across wrist joints. In terms of DSC, SwinUMamba consistently outperforms other models across nearly all regions (e.g., 0.988 on the 1st Metacarpal and 0.986 on the Radius), indicating highly accurate overlap with ground truth. Other models such as UMambaEnc, TransUNet, and UNet++ also show strong and stable performance, particularly on larger or less ambiguous joints.

However, NSD scores in Table 9 reveal greater performance variability at the boundary level. Difficult regions such as the Tz and Tr exhibit noticeable drops in accuracy (e.g., NSD < 0.7 in many models), reflecting the challenges of segmenting small, overlapping, or irregularly shaped bones. Despite this, SwinUMamba maintains the highest NSD scores across most joints (e.g., 0.987 on the Ulna, 0.973 on the 1st Metacarpal), demonstrating strong robustness in anatomically complex areas.

Table 10 and Table 11 provide a comparative analysis between joints with and without BE. Across nearly all models and joints, segmentation performance is lower in BE-affected samples, especially in the 1st Metacarpal, Lunate, and Scaphoid, which are commonly affected in the early stages of RA. Statistically significant differences ($p < 0.05$ to $p < 0.001$) are observed for most models, confirming

Table 8: DSC Model performance on all joints. The best results in each column are highlighted in **bold**, and the second-best values are underlined.

Model	Cap	Radius	Ulna	Ham	Lu	Tri	Sca	Tr	Tz	MC1	MC2	MC3	MC4	MC5
Unet	0.958	0.978	0.981	0.953	0.949	0.964	0.962	0.948	0.933	0.975	0.974	0.962	0.970	0.975
DeepLabV3	0.965	0.981	0.978	0.959	0.955	0.959	0.965	0.950	0.936	0.979	0.976	0.968	0.971	0.975
FPN	0.961	0.979	0.980	0.953	0.952	0.958	0.961	0.947	0.926	0.976	0.977	0.968	0.972	0.974
PSPNet	0.944	0.971	0.965	0.943	0.931	0.946	0.948	0.931	0.911	0.960	0.965	0.954	0.959	0.965
DeepLabV3+	0.964	0.982	0.983	0.956	0.953	0.963	0.965	0.950	0.932	0.981	0.978	0.970	0.975	0.978
SegResNet	0.953	0.976	0.980	0.945	0.952	0.957	0.961	0.941	0.929	0.974	0.965	0.962	0.968	0.972
Unet++	0.970	0.982	0.987	0.963	0.957	0.971	0.972	0.958	0.942	0.983	0.983	0.973	0.979	0.980
SegFormer	0.965	0.982	0.983	0.959	0.956	0.966	0.965	0.952	0.935	0.980	0.979	0.970	0.975	0.977
TransUNet	0.974	0.985	0.989	0.969	0.965	0.972	0.975	0.961	0.945	0.987	0.985	0.974	0.982	0.983
UKAN	0.964	0.981	0.982	0.958	0.957	0.963	0.967	0.952	0.934	0.980	0.979	0.971	0.975	0.978
UMambaBot	0.970	0.984	0.986	0.966	0.963	0.970	0.973	0.960	0.946	0.985	0.984	0.975	0.981	0.982
UMambaEnc	0.973	0.985	0.988	0.967	0.965	0.973	0.974	0.962	0.944	0.986	0.984	0.975	0.981	0.982
SwinUMamba	0.976	0.986	0.990	0.971	0.966	0.974	0.978	0.965	0.949	0.988	0.986	0.978	0.983	0.984

Table 9: NSD performance on all joints. The best results in each column are highlighted in **bold**, and the second-best values are underlined.

Model	Cap	Radius	Ulna	Ham	Lu	Tri	Sca	Tr	Tz	MC1	MC2	MC3	MC4	MC5
Unet	0.707	0.790	0.946	0.705	0.723	0.828	0.793	0.693	0.648	0.897	0.890	0.818	0.885	0.911
DeepLabV3	0.744	0.802	0.918	0.730	0.734	0.784	0.789	0.685	0.656	0.916	0.904	0.843	0.904	0.915
FPN	0.686	0.774	0.932	0.669	0.703	0.773	0.754	0.659	0.569	0.882	0.892	0.820	0.890	0.896
PSPNet	0.543	0.667	0.789	0.594	0.561	0.648	0.632	0.521	0.492	0.755	0.798	0.721	0.792	0.811
DeepLabV3+	0.730	0.814	0.956	0.710	0.717	0.822	0.801	0.696	0.615	0.924	0.910	0.848	0.906	0.926
SegResNet	0.671	0.764	0.937	0.674	0.740	0.789	0.784	0.659	0.623	0.882	0.854	0.803	0.862	0.884
Unet++	0.812	0.838	0.973	0.784	0.769	0.882	0.857	0.759	0.706	0.931	0.938	0.863	0.932	0.942
SegFormer	0.752	0.817	0.962	0.749	0.741	0.850	0.795	0.713	0.652	0.916	0.914	0.851	0.913	0.928
TransUNet	0.848	0.871	0.983	0.840	0.809	0.894	0.888	0.783	0.730	0.963	0.946	0.870	0.953	0.963
UKAN	0.741	0.804	0.949	0.727	0.753	0.822	0.819	0.710	0.637	0.917	0.908	0.844	0.906	0.921
UMambaBot	0.819	0.864	0.972	0.809	0.813	0.879	0.887	0.778	0.746	0.950	0.942	0.878	0.945	0.958
UMambaEnc	0.835	0.875	0.980	0.817	0.819	0.899	0.883	0.789	0.735	0.960	0.942	0.877	0.943	0.956
SwinUMamba	0.866	0.895	0.987	0.859	0.824	0.911	0.910	0.824	0.765	0.973	0.958	0.896	0.963	0.970

Table 10: DSC performance on representative wrist bones. (Mann-Whitney U test between BE & nonBE, *: $P < 0.05$, **: $P < 0.01$, ***: $P < 0.001$).

Model	Radius			Ulna			Lunate			Scaphoid			Trapezium			MC1		
	BE	nonBE	P	BE	nonBE	P	BE	nonBE	P	BE	nonBE	P	BE	nonBE	P	BE	nonBE	P
Unet	0.977	0.978		0.985	0.981		0.943	0.949		0.969	0.959		0.940	0.950		0.961	0.977	**
DeepLabV3	0.978	0.981	*	0.978	0.978		0.950	0.955		0.965	0.965		0.946	0.951	*	0.974	0.980	*
FPN	0.972	0.979		0.982	0.980		0.949	0.952		0.965	0.959		0.939	0.949	*	0.970	0.977	
PSPNet	0.972	0.971		0.962	0.966		0.895	0.932		0.952	0.947		0.929	0.931		0.946	0.961	**
DeepLabV3+	0.976	0.982		0.987	0.983		0.945	0.954		0.970	0.964		0.944	0.951		0.977	0.981	*
SegResNet	0.968	0.976		0.981	0.980		0.938	0.952		0.967	0.959		0.935	0.942		0.963	0.975	**
Unet++	0.980	0.982		0.990	0.987		0.949	0.957		0.975	0.971		0.954	0.959		0.979	0.983	**
SegFormer	0.980	0.982		0.985	0.983		0.953	0.956		0.969	0.963		0.946	0.953	*	0.974	0.980	*
TransUNet	0.982	0.985		0.990	0.989		0.963	0.965	*	0.977	0.974		0.959	0.962		0.981	0.988	*
UKAN	0.978	0.981		0.985	0.982		0.944	0.957		0.970	0.966		0.949	0.953		0.973	0.981	
UMambaBot	0.980	0.984		0.989	0.986		0.974	0.963		0.977	0.972		0.956	0.961	*	0.979	0.986	***
UMambaEnc	0.981	0.985	*	0.991	0.988		0.970	0.965		0.978	0.972		0.957	0.963	*	0.981	0.986	**
SwinUMamba	0.982	0.987		0.991	0.990		0.974	0.966		0.981	0.977		0.962	0.966		0.983	0.989	*

that BE degrades segmentation accuracy in disease-sensitive joints. For instance, SwinUMamba’s DSC on the 1st Metacarpal drops from 0.983 to 0.928 in the presence of BE, with similar trends seen in UMambaBot and TransUNet.

The effect of BE is even more significant in NSD results, where boundary accuracy declines notably in BE cases. Some models (e.g., PSPNet, DeepLabV3) show particularly poor performance under BE, especially in the Lunate and Scaphoid, underscoring the difficulty of segmenting deformed or eroded bone boundaries. Nonetheless, models such as SwinUMamba and UMambaEnc remain more robust, maintaining relatively high NSD scores even in BE cases (e.g., 0.944 on the 1st Metacarpal), suggesting better generalization to abnormal anatomical structures.

Table 11: NSD performance on representative wrist bones. (Mann-Whitney U test between BE & nonBE, *: P < 0.05; **: P < 0.01; ***: P < 0.001).

Model	Radius			Ulna			Lunate			Trapezium			Scaphoid			MC1		
	BE	nonBE	P	BE	nonBE	P	BE	nonBE	P	BE	nonBE	P	BE	nonBE	P	BE	nonBE	P
UNet	0.765	0.791		0.956	0.945		0.594	0.726		0.678	0.696		0.829	0.779		0.849	0.902	**
DeepLabV3	0.757	0.803		0.933	0.917		0.616	0.737		0.681	0.686		0.794	0.788		0.887	0.919	*
FPN	0.647	0.777		0.950	0.931		0.548	0.706		0.633	0.665		0.782	0.744		0.845	0.885	
PSPNet	0.632	0.668		0.802	0.788		0.339	0.566		0.546	0.516		0.646	0.626		0.720	0.758	
DeepLabV3+	0.742	0.816		0.974	0.954		0.547	0.721		0.679	0.699		0.841	0.786		0.909	0.926	*
SegResNet	0.676	0.766		0.938	0.937		0.581	0.743		0.674	0.656		0.818	0.771		0.817	0.888	**
UNet++	0.796	0.838		0.986	0.972		0.596	0.773	*	0.770	0.756		0.880	0.848		0.915	0.933	**
SegFormer	0.817	0.817		0.972	0.962		0.623	0.743		0.708	0.714		0.839	0.778		0.891	0.919	
TransUNet	0.801	0.873		0.989	0.983		0.741	0.810	*	0.794	0.781		0.893	0.886		0.934	0.966	
UKAN	0.735	0.806		0.953	0.949		0.667	0.755		0.729	0.706		0.839	0.811		0.889	0.920	
UMambaBot	0.791	0.865		0.981	0.971		0.801	0.814		0.794	0.775		0.907	0.880		0.928	0.953	**
UMambaEnc	0.800	0.877		0.986	0.980		0.773	0.821		0.798	0.787		0.905	0.874		0.925	0.963	*
SwinUMamba	0.828	0.897		0.997	0.986		0.825	0.824		0.842	0.820		0.925	0.905	*	0.944	0.976	

Table 12: Overlap DSC performance on overlapping regions. The best results in each column are highlighted in **bold**, and the second-best values are underlined.

Model	Radius-Sca	Radius-Lu	Sca-Tr	Cap-Sca	Tz-MC1	Cap-MC3	Ham-MC4	Lu-Sca	Tr-Tz	Cap-Tz	Ham-MC5	Tr-MC2	Tz-MC2	MC2-MC3	Mean
UNet	0.721	0.760	0.623	0.825	0.600	0.352	0.327	0.727	0.874	0.441	0.816	0.754	0.205	0.528	0.624
DeepLabV3	0.739	0.797	0.644	0.846	0.706	0.486	0.518	0.753	0.885	0.542	0.836	0.760	0.275	0.643	0.684
FPN	0.708	0.775	0.636	0.822	0.647	0.421	0.496	0.749	0.864	0.511	0.805	0.739	0.280	0.632	0.658
PSPNet	0.671	0.692	0.577	0.750	0.541	0.302	0.426	0.686	0.834	0.477	0.774	0.691	0.285	0.576	0.600
DeepLabV3+	0.746	0.789	0.648	0.834	0.643	0.476	0.523	0.741	0.877	0.534	0.825	0.748	0.275	0.653	0.675
SegResNet	0.719	0.758	0.603	0.850	0.202	0.000	0.000	0.736	0.876	0.433	0.762	0.072	0.086	0.416	0.478
UNet++	0.764	0.811	0.684	0.876	0.697	0.495	0.445	0.779	0.891	0.540	0.837	0.798	0.294	0.590	0.690
SegFormer	0.739	0.797	0.663	0.833	0.713	0.464	0.484	0.756	0.881	0.542	0.837	0.756	0.288	0.656	0.683
TransUNet	<u>0.798</u>	<u>0.845</u>	0.710	<u>0.890</u>	<u>0.749</u>	0.247	<u>0.617</u>	0.796	0.900	<u>0.587</u>	<u>0.875</u>	<u>0.810</u>	<u>0.313</u>	0.669	0.710
UKAN	0.738	0.810	0.655	0.848	0.665	0.382	0.417	0.759	0.882	0.464	0.840	0.763	0.253	0.560	0.658
UMambaBot	0.787	0.842	<u>0.714</u>	0.887	0.742	0.518	0.568	<u>0.806</u>	<u>0.901</u>	0.581	0.870	0.802	0.274	<u>0.674</u>	<u>0.723</u>
UMambaEnc	0.784	0.841	0.701	0.884	0.742	<u>0.531</u>	0.606	<u>0.805</u>	<u>0.904</u>	0.562	0.860	0.798	0.291	0.670	<u>0.723</u>
SwinUMamba	0.806	0.866	0.725	0.904	0.767	0.597	0.640	0.831	0.907	0.599	0.879	0.837	0.337	0.685	0.751

Table 12 and Table 13 demonstrate the challenge of accurately segmenting overlapping regions among wrist bones. Among all methods, SwinUMamba achieves the best overall performance, yielding mean overlap DSC and NSD values of 0.751 and 0.754, respectively. It ranks first in almost every pairwise region; for example, the Radius–Lu interface (0.866 DSC, 0.829 NSD) and the Cap–Sca interface (0.904 DSC, 0.871 NSD), indicating that its global-context modelling enables precise delineation along complex boundaries. The next tier comprises UMambaEnc, UMambaBot, and TransUNet. These models trail SwinUMamba by only three to four percentage points on average yet clearly surpass purely convolutional baselines, implying that integrating long-range attention or state-space mechanisms with local convolutions improves the separation of tightly packed structures. Classical CNN backbones (UNet, DeepLabV3, FPN, SegFormer) exhibit greater performance variance, and SegResNet records the lowest mean scores because it underperforms on Ham-related interfaces. Comparing DSC with NSD reveals that most methods sacrifice little accuracy when boundary sensitivity increases, whereas SwinUMamba retains nearly identical values, indicating stable edge fidelity. Conversely, TransUNet increases its NSD on the Cap–MC3 interface despite a low DSC, which suggests conservative predictions that conform closely to true borders while underestimating volume.

The visualization in Fig. 9 also shows similar results. Compared to the ground truth, all models exhibit varying degrees of segmentation degradation, particularly along bone boundaries characterized by anatomical overlap or low-contrast regions. This issue is most evident in carpal bones such as the Trapezium and Trapezoid, where multi-layer occlusions and irregular bone geometry lead to fragmented or discontinuous predictions. Meanwhile, considerable visual inconsistency can be observed across models when segmenting BE-affected regions. The inward collapse and morphological distortion caused by BE (RA) are often under-segmented or misrepresented, reflecting a general lack of robustness in handling pathological changes. While some models yield smoother contours or more complete shapes in isolated cases, no architecture consistently addresses these challenges across all scenarios.

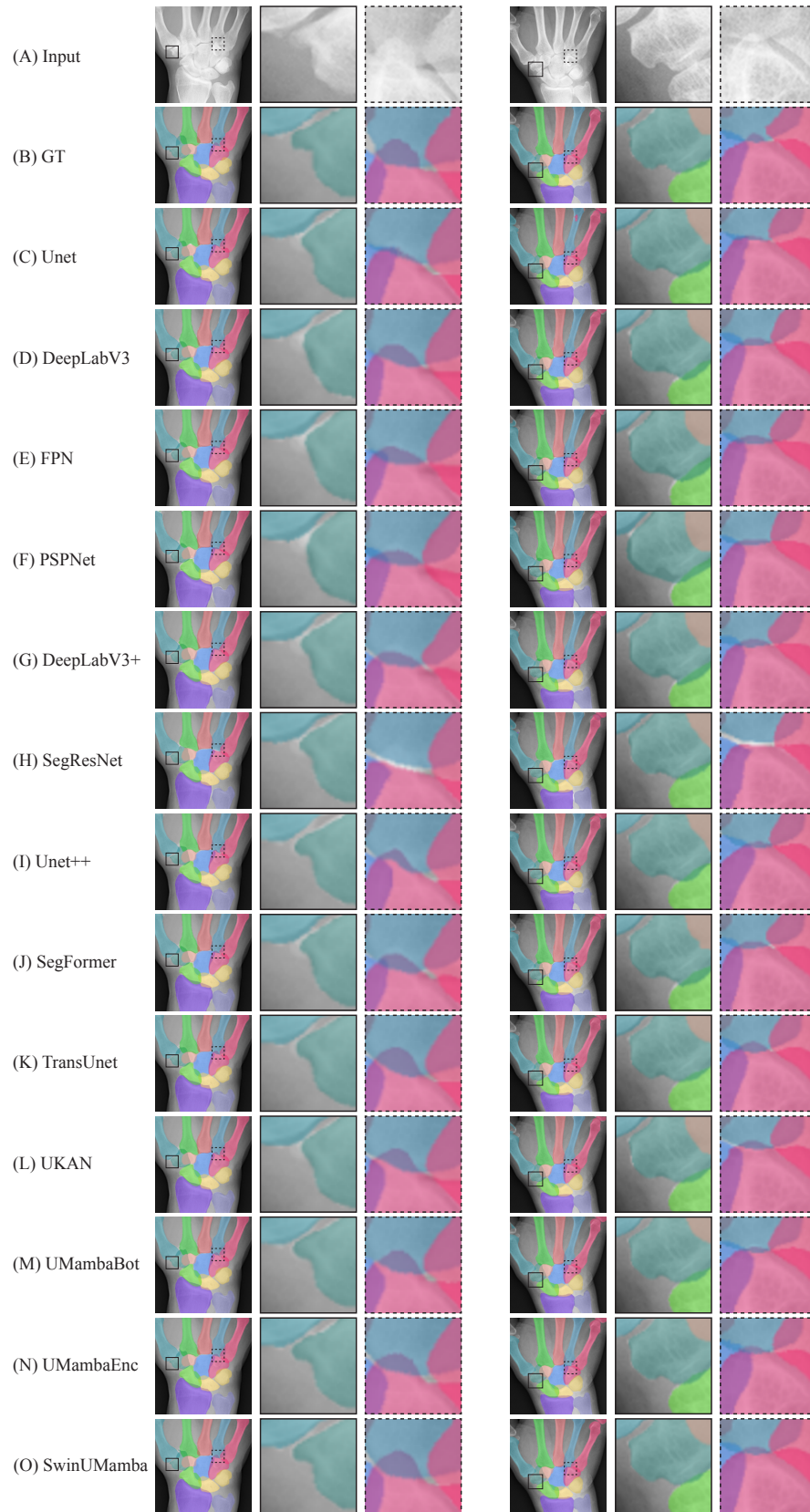


Figure 9: Additional visual results for wrist bone segmentation.

Table 13: Overlap NSD performance on overlapping regions. The best results in each column are highlighted in **bold**, and the second-best values are underlined.

Model	Radius-Sca	Radius-Lu	Sca-Tr	Cap-Sca	Tz-MC1	Cap-MC3	Ham-MC4	Lu-Sca	Tr-Tz	Cap-Tz	Ham-MC5	Tr-MC2	Tz-MC2	MC2-MC3	Mean
UNet	0.677	0.641	0.636	0.680	0.619	0.588	0.478	0.625	0.608	0.622	0.638	0.570	0.400	0.577	0.598
DeepLabV3	0.671	0.669	0.653	0.717	0.705	0.620	0.557	0.661	0.618	0.634	0.686	0.552	0.411	0.668	0.631
FPN	0.636	0.639	0.619	0.627	0.616	0.555	0.533	0.632	0.537	0.583	0.618	0.514	0.394	0.625	0.581
PSPNet	0.551	0.505	0.549	0.479	0.514	0.483	0.490	0.500	0.446	0.544	0.549	0.446	0.380	0.545	0.498
DeepLabV3+	0.669	0.645	0.653	0.674	0.614	0.612	0.556	0.617	0.584	0.612	0.655	0.544	0.397	0.660	0.607
SegResNet	0.670	0.656	0.615	0.735	0.340	0.000	0.000	0.619	0.602	0.629	0.557	0.106	0.254	0.556	0.460
UNet++	0.735	0.725	0.715	0.796	0.723	0.650	0.558	0.697	0.664	0.685	0.728	0.649	0.472	0.657	0.677
SegFormer	0.674	0.675	0.661	0.676	0.711	0.617	0.546	0.661	0.610	0.648	0.698	0.555	0.413	0.658	0.630
TransUNet	<u>0.797</u>	0.783	0.715	0.844	0.759	0.533	<u>0.684</u>	0.733	0.704	<u>0.698</u>	<u>0.797</u>	<u>0.672</u>	0.460	0.706	0.709
UKAN	0.700	0.699	0.670	0.719	0.671	0.575	0.474	0.674	0.606	0.596	0.707	0.574	0.413	0.630	0.623
UMambaBot	0.791	0.783	0.742	<u>0.845</u>	<u>0.764</u>	0.657	0.605	<u>0.764</u>	0.709	0.693	0.785	0.660	0.459	<u>0.723</u>	0.713
UMambaEnc	0.789	<u>0.794</u>	<u>0.743</u>	0.832	0.762	<u>0.684</u>	0.655	0.741	<u>0.717</u>	0.692	0.757	0.660	<u>0.480</u>	0.703	<u>0.717</u>
SwinUMamba	0.818	0.829	0.779	0.871	0.815	0.701	0.701	0.792	0.741	0.711	0.807	0.735	0.493	0.736	0.754

C.2 Classification of BE

Figure 10 presents a visual comparison of binary classification predictions for joints with and without BE. While most models demonstrate strong performance on nonBE regions, substantial misclassification is observed in BE cases, particularly in models such as MobileNet and ResNet, which frequently misclassify BE joints as nonBE. This indicates a tendency toward conservative predictions and highlights the challenges in detecting pathological variations. BE regions, often characterized by irregular contours and structural degradation, remain difficult for all models to classify accurately. Although recent architectures such as MedMamba and ConvKAN show partial improvements in BE sensitivity, consistent and precise discrimination of BE remains an unresolved challenge. These results underscore the need for model architectures capable of capturing subtle morphological changes and learning robust feature representations under pathological conditions.

D Broader Impact

This work provides a publicly available and well-annotated multi-task wrist dataset and benchmark designed to advance research in RA diagnosis using conventional wrist radiographs. This resource enables researchers to build and evaluate advanced models for RA-related tasks with consistency and rigor. The authors do not anticipate any negative societal impacts stemming from this work. On the contrary, a positive impact may arise through the development of robust computer-aided diagnosis systems, which can facilitate early detection and monitoring of RA with reduced reliance on manual annotations. This has the potential to enhance clinical efficiency, reduce expert workload, and improve access to specialized care, particularly in under-resourced healthcare settings.

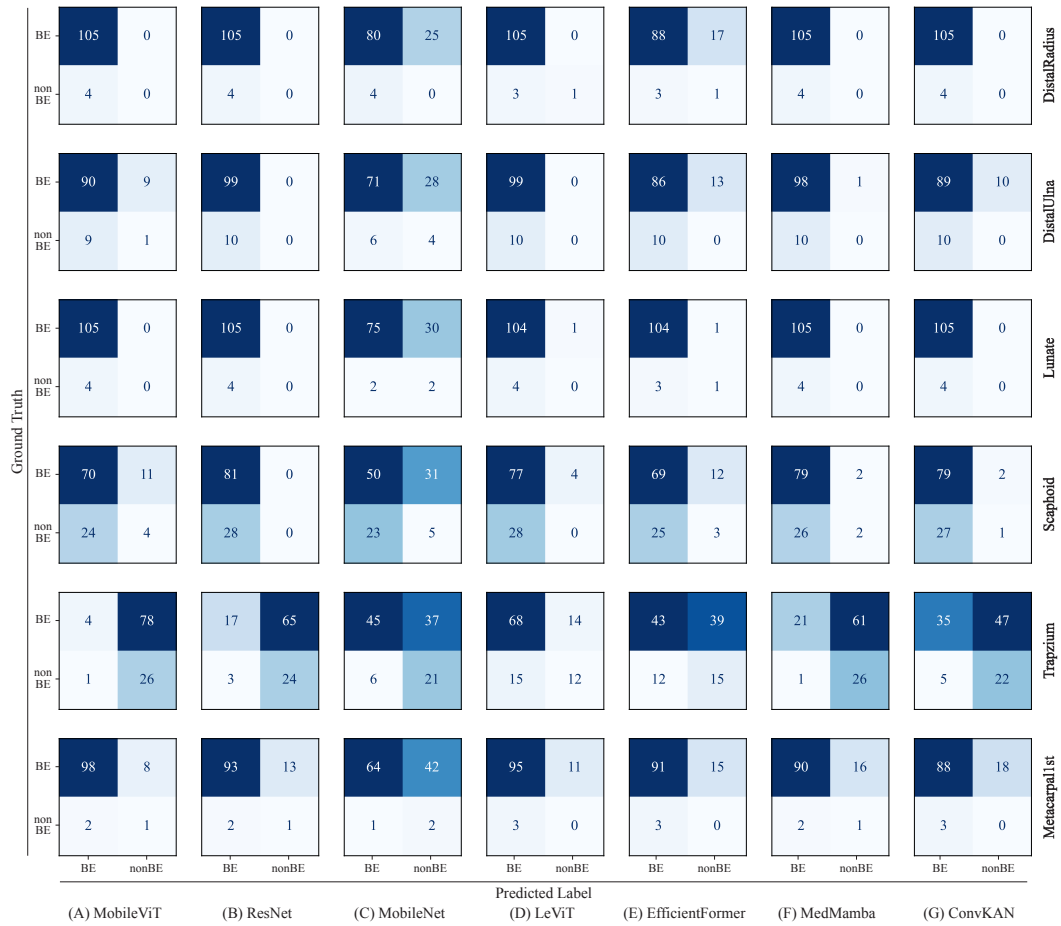


Figure 10: Confusion matrix results for classification of BE and nonBE.